ACS Sustainable Chemistry & Engineering

pubs.acs.org/journal/ascecg

Research Article

High-Throughput Fluorescent Screening and Machine Learning for Feature Selection of Electrocatalysts for the Alkaline Hydrogen Oxidation Reaction

Jeremy L. Hitt, Dasol Yoon, Jeffrey R. Shallenberger, David A. Muller, and Thomas E. Mallouk*

Cite This: https://doi.org/10.1021/acssuschemeng.2c05170

Read Online

ACCESS | Metrics & More | Article Recommendations | Supporting Information

ABSTRACT: A parallel fluorescent screening method was used to evaluate active catalysts for the alkaline hydrogen oxidation reaction (HOR). A library of 1584 catalyst samples containing single element, binary, and ternary combinations was prepared in high-throughput fashion from 12 elements (Pt, Ag, Au, Co, Cu, Fe, Hg, Ni, Pb, Pd, Rh, and Sn) and was screened for their HOR onset potentials in an alkaline electrolyte. One of the most active alloys, Pt_6Sn_4, was tested in an alkaline polymer membrane fuel cell and produced a power density of 132 mW/(cm^2·mg of Pt) compared with 103 mW/(cm^2·mg of Pt) for a Pt/C reference catalyst. The compositions, morphologies, surface chemistries, and atomic structures of the catalysts were characterized to better understand the trends in their properties. The HOR onset potentials measured in the screening experiments were then used to create a database that was combined with elemental descriptors to train several machine learning models. The most accurate models were used to predict new alloy catalysts and rank the importance of each feature in the data set.

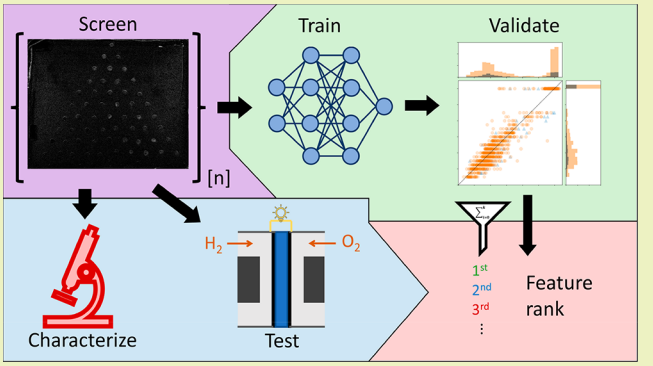

KEYWORDS: *Alloy electrocatalyst, Hydrogen oxidation, Alkaline fuel cell, High-throughput screening, Machine learning, Activity descriptor*

Downloaded via CORNELL UNIV on November 30, 2022 at 21:13:51 (UTC).
See https://pubs.acs.org/sharingguidelines for options on how to legitimately share published articles.

INTRODUCTION

The successful transition of the world's energy economy from fossil fuels to renewable resources will depend on the development of cost-effective technologies for energy storage. While the cost per watt-hour of building and operating solar and wind capacity has dropped below the cost of new fossil fuel and nuclear power plants for electricity generation,[1] wind and solar are intermittent power sources. A reliable electrical grid based primarily on renewables will thus require inexpensive energy storage to be available at a very large scale.[2] Electrochemical technologies including Li ion batteries, metal−air batteries, and redox-flow batteries are promising for short-term energy storage, but they become cost-prohibitive for seasonal storage. For this reason, there is much current interest in developing hydrogen as an energy carrier and an energy storage vehicle, since it can be generated by electrolysis of water, used as a feedstock to synthesize liquid fuels, or converted back to electrical power by combustion or oxidation in fuel cells. Hydrogen-powered fuel cells also potentially provide an alternative to battery technology for transportation sectors that are difficult to electrify, such as long-haul trucking.[3]

Anion exchange membrane fuel cells (AEMFCs) and electrolyzers have the potential to displace acidic polymer electrolyte membrane (PEM) fuel cells and electrolyzers because, in principle, they enable the replacement of expensive and rare platinum group metal (PGM) electrocatalysts by earth-abundant catalysts.[4] Some promising recent discoveries of PGM-free catalysts for AEMFCs are the $MnCoO_x$ spinel cathode catalysts studied by Yang et al.,[5] which achieved power densities of over 1 W/cm^2, and the atomically dispersed cathode catalysts studied by Zelenay et al.,[6−8] which gave power densities up to 600 mW/cm^2. The latter used Fe−N−C or Co−N−C groups embedded in graphitic carbon to catalyze the oxygen reduction reaction. However, a persistent challenge in the development of efficient AEMFCs is the sluggish reaction kinetics of the alkaline hydrogen oxidation reaction (HOR). Studies of the HOR reaction at different pH values have shown that the exchange current density is approximately 2 orders of magnitude lower in base than in acid at Pt

Received: August 29, 2022
Revised: November 12, 2022

© XXXX American Chemical Society

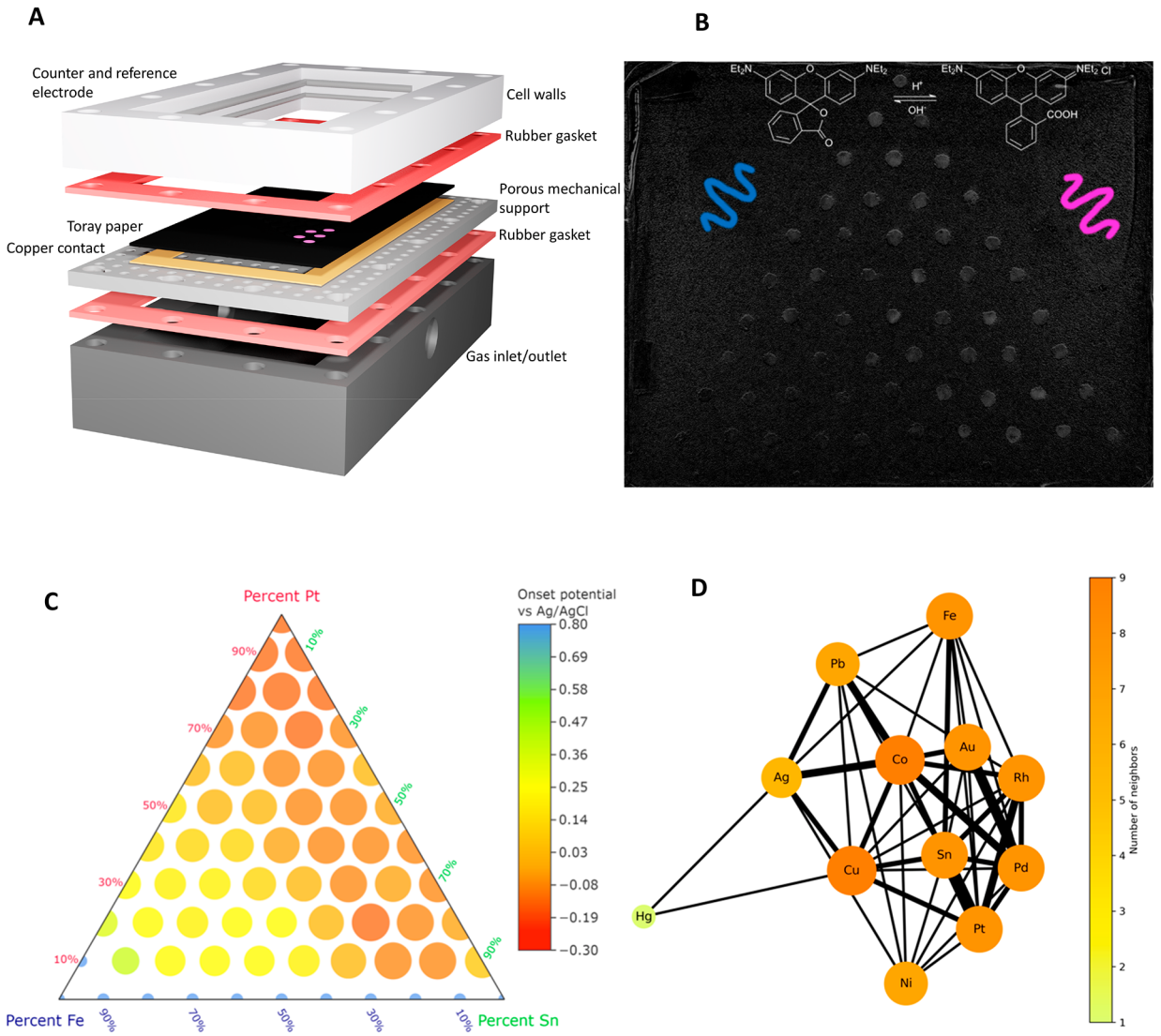

Figure 1. (A) Electrochemical cell used for high-throughput screening. From bottom to top: gas chamber, silicone gasket, porous mechanical support, copper electrical contact, Toray carbon paper with alloy catalysts, silicone gasket, PTFE cell walls, platinum counter electrode, AgCl pseudoreference electrode. (B) Grayscale image of an alloy catalyst array under anodic potential in a hydrogen saturated electrolyte. The diagram at the top shows the pH photoswitching fluorescence of rhodamine B. (C) Example of a ternary heat map of the onset potential constructed from the digital images. The potential is reported with respect to the AgCl pseudoreference electrode. (D) Spring graph network created from all the samples in the data set. Each connection signifies that the two elements are present in an array, and the size and color of each node represent how many connections it has. The distance of each node from the center of the network represents the strength of its overall connectivity.

electrodes.[9−11] In acidic electrolytes, the relationship between the adsorption energy of H atoms and catalytic activity follows a volcano plot as expected from the Sabatier principle.[12] Under basic conditions, the situation is more complex. While all proposed microkinetic models for the alkaline HOR on Pt involve the same intermediate, namely adsorbed H atoms (H_{ads}), there are competing explanations for the slow kinetics. Modifications to Pt and to other single element catalysts have been shown to increase the HOR activity. For example, Markovic and co-workers studied the activities of Pt−Ru alloys and $Ni(OH)_2$-modified Pt for the alkaline HOR and found that they were considerably more active than pure Pt. The enhancement in the HOR kinetics was attributed to the oxophilicity of Ru and Ni, which were thought to assist in the adsorption of reactive OH^- ions.[13] In contrast, Zhuang et al. have ascribed the catalytic enhancement to a change in electronic structure and in the H adsorption energy, supported by a shift in the voltammetric peaks.[14] Koper et al. studied the alkaline HOR at Pt with metal atoms adsorbed onto the surface and found that the HOR activation energy correlated with OH adsorption strength.[15] While this is consistent with the bifunctional catalysis model proposed by Markovic et al., both computational and experimental studies suggest an alternative picture in which oxophilic adatoms alter the orientation and hydrogen bonding of water molecules at the catalytic interface.[16−20]

Recently, the search for improved alloy HOR catalysts has been extended to Pt alloy compositions that contain a broad range of transition elements (including Fe,[21,22] Co,[21,22] Ru,[21,22] Pd,[21,23,24] Rh,[21,25] Cu,[21,22] Ni,[21] Ir,[23−25] and Au[22]), as well as metal oxide supported alloys.[26,27] Given the very large number of possible combinations of these components and the still-evolving science of the alkaline HOR, there is an opportunity to use high-throughput methods[28−35] to evaluate alloy

https://doi.org/10.1021/acssuschemeng.2c05170
ACS Sustainable Chem. Eng. XXXX, XXX, XXX−XXX

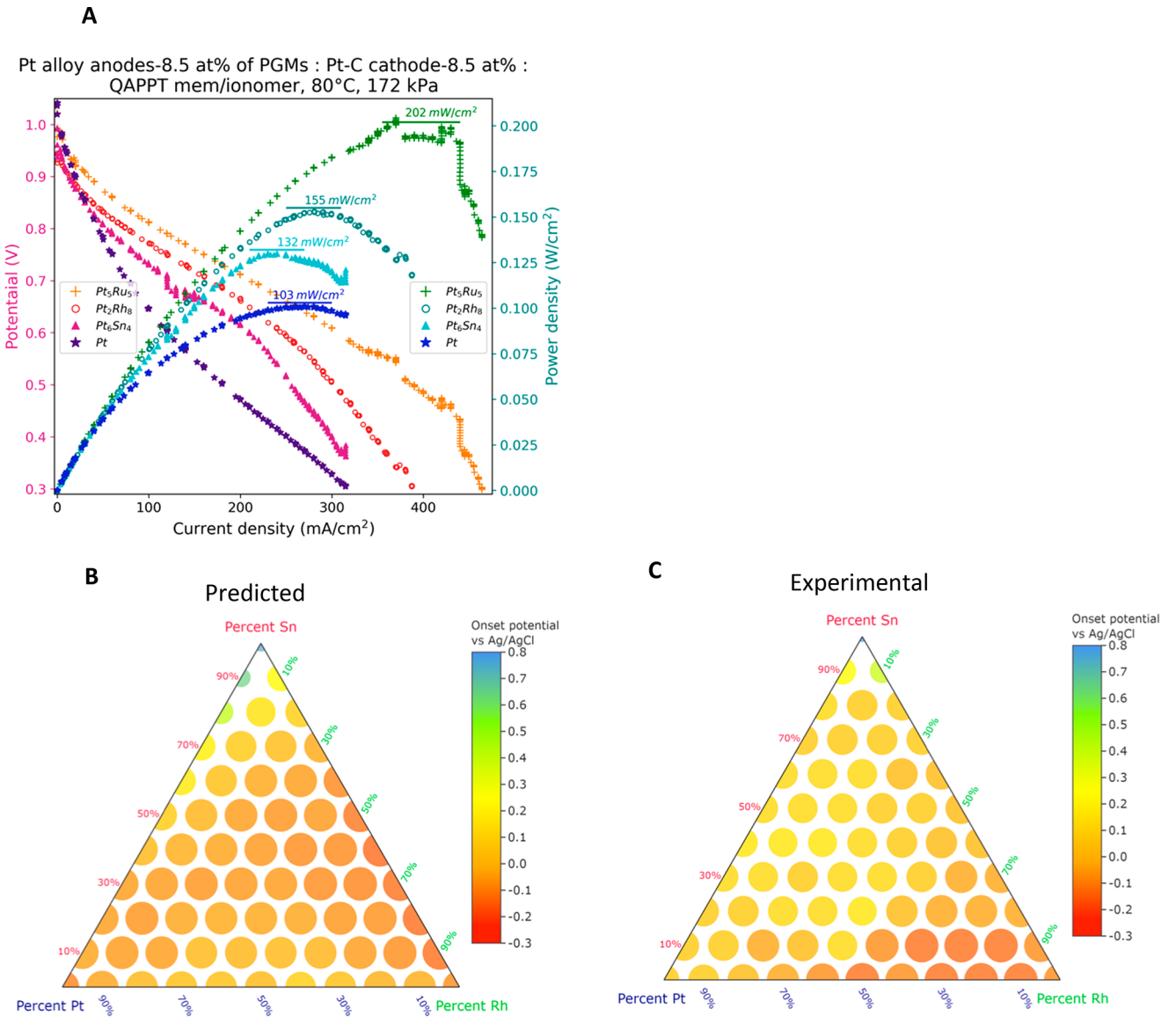

Figure 2. (A) Fuel cell polarization curves and power curves with different Pt containing anode catalysts. Each MEA contains 0.5 mg of Pt/cm^2 on the cathode and 2.58 mmol of PGM/cm^2 on the anode. This anode mass loading for the pure Pt/C anode is equivalent to 0.5 mg of Pt/cm^2. (B) Predicted onset potential from the neural network of alkaline HOR for a SnPtRh array. (C) Experimental onset potential of SnPtRh array recorded from the screening experiment. A small difference is present, mostly on the Pt−Rh binary line. The parity plot for this prediction is shown in Figure S11.

electrocatalysts systematically and learn from possible trends in activity. High-throughput computational screening of electrocatalysts has been increasingly enabled by advances in computational modeling of electrochemical interfaces, but the results from that approach are often very different from those found in experimental systems. In contrast, high-throughput experimentation coupled with computation enables researchers to create large libraries of electrochemical data that can be used to train and test active machine learning models.[36−38] These models are useful not only for predicting new catalyst compositions but also for discovering patterns in the data that describe the kinetic processes and thus lead to a deeper understanding.[39,40] Here, we evaluate this approach with a relatively small library of 1584 alloy catalysts to sample a large composition space for alkaline HOR catalysis. We used a previously described parallel screening method[28,29,33] to measure the onset potential of hydrogen oxidation in ternary arrays that each consisted of 66 discrete compositions. Out of the possible ternary compositions of 12 elements (220 ternary arrays), we chose 24, i.e., 11% of the total composition space. The resulting data were used to train three different machine learning algorithms and predict new alloys that are active for the alkaline HOR. In addition to finding highly active catalysts, we also tested different methods for extracting the feature importance in the models to discover which attributes are the most relevant descriptors of electrocatalyst activity.

EXPERIMENTAL SECTION

High-Throughput Screening. Each array of carbon-supported HOR catalysts was made by coreducing metal salts in appropriate proportions to make a triangular plot of 66 unique compositions as previously described.[28,33] Metal precursor solutions were made by dissolving 0.025 mmol of the appropriate metal nitrate or chloride in 3 mL of Nanopure water and 2 mL of acetonitrile. A 7 mg amount of Vulcan XC-72 carbon was added to each solution followed by 25 μL

https://doi.org/10.1021/acssuschemeng.2c05170
ACS Sustainable Chem. Eng. XXXX, XXX, XXX−XXX

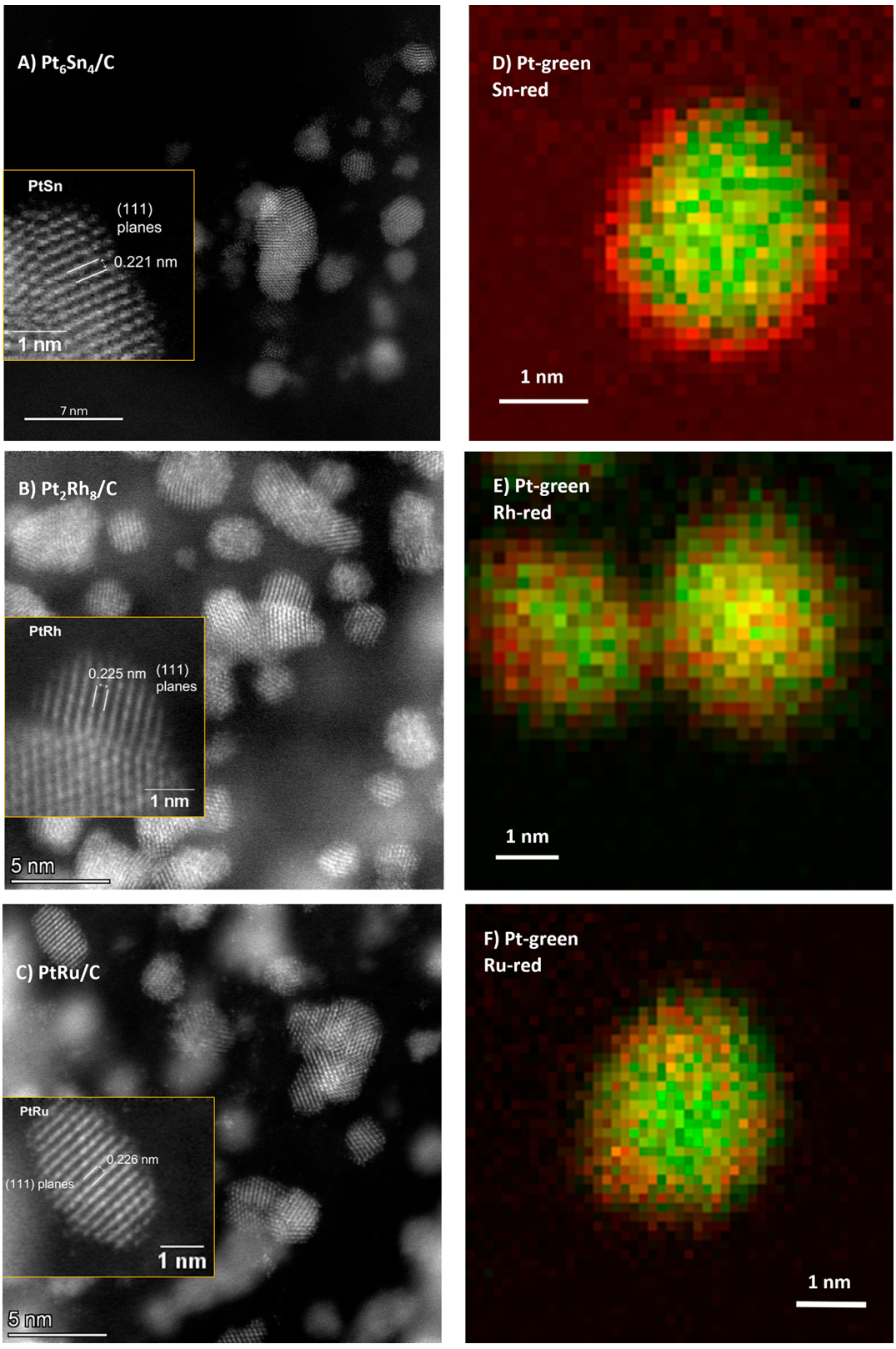

Figure 3. STEM images of (A) Pt_6Sn_4/C, (B) Pt_2Rh_8/C and (C) PtRu/C with insets showing the particles used for structural analysis. Each image was acquired at 300 kV. EDS maps of (D) Pt_6Sn_4/C, (E) Pt_2Rh_8/C, and (F) PtRu/C acquired at 60 kV. Maps show that Rh and Ru are homogeneously mixed with Pt, but Sn appears to be more concentrated around the outside of the particle.

of 5 wt % Nafion in alcohol/water (Sigma-Aldrich Nafion 117 solution). The solutions were sonicated in a water bath for 10 min with occasional stirring. The solutions were pipetted onto Toray carbon paper 090, 5% PTFE treated (Fuel Cell Store) using a Gilson PipetMax 268 in the ratios required to produce the composition map illustrated in Figure 1. After dispensing of all the metal precursors and

https://doi.org/10.1021/acssuschemeng.2c05170
ACS Sustainable Chem. Eng. XXXX, XXX, XXX−XXX

generation of the target compositions, each sample location had a combined loading of 1×10^{-4} mmol of metal ions. Next, a drop of excess, aqueous sodium borohydride (2.6×10^{-3} mmol/drop) was added at each location to reduce the salts to their metallic forms. The array was dried at 70 °C in air for several hours and then gently submerged in a beaker of Nanopure water to rinse away the remaining reactants and ionic products. An electrolyte was prepared by using 150 mL of acetonitrile, 3 mg of rhodamine B (Sigma-Aldrich), 5 g of tetrabutylammonium perchlorate (Sigma-Aldrich), and 1 mL of Nanopure water. The solution was stirred until everything was dissolved and well-mixed. Then 33 μL of 20 wt % tetraethylammonium hydroxide was added and the solution was stirred again. The array was placed in the home-built screening cell illustrated in Figure 1A, and the electrolyte was added on top. Hydrogen gas was purged through the cell electrolyte for 5 min and then stopped. Immediately thereafter, a potential step scan was applied to the cell from −0.4 to 0.5 V versus a Ag/AgCl pseudoreference electrode. Each step had a size of 50 mV, and the potential was held for 2 s before advancing to the next step. For arrays that did not contain any Pt, Pd, or Rh, the potential was scanned from −0.1 to 0.8 V versus a Ag/AgCl pseudoreference electrode. The pseudoreference electrode was made by anodizing Ag wire in 1 M KCl at ∼1 mA/cm^2 until a dark gray film appeared on the wire. The electrode was calibrated by ensuring that the potential difference between the pseudoreference and a standard Ag/AgCl reference was less than 0.008 V. The pseudoreference electrode was stored in a saturated KCl solution between experiments. The screening experiments were done in a darkened fume hood where a digital camera (Canon EOS 77D) was positioned above the cell and programmed to take a photograph every 2 s, synchronized with the potential steps. To determine the onset potential of each catalyst spot, all images were analyzed using a Python program described in more detail in the Supporting Information. A sample of the images after processing is shown in Figure 1B along with a schematic drawing of the pH dependent fluorescence mechanism of rhodamine B.

Fuel Cell Testing and Material Characterization. To test the validity of the high-throughput-screening results, we chose two compositions that had low HOR onset overpotentials (Pt_2Rh_8, Pt_6Sn_4) in the screening experiments and used them to fabricate membrane−electrode assemblies (MEAs) that were then tested in an AEMFC, as shown in Figure 2. To synthesize the reference Pt/C catalyst, 53.99 mg of potassium hexachloroplatinate (Alfa Aesar) was added to 3 mL of Nanopure water and 2 mL of acetonitrile. The alloy catalysts were made by adjusting the starting salt compositions accordingly. The Pt_2Rh_8 catalyst was prepared by combining 23.16 mg of rhodium chloride trihydrate (Alfa Aesar) and 10.68 mg of potassium hexachloroplatinate. For Pt_6Sn_4, 53.99 mg of potassium hexachloroplatinate was used along with 13.88 mg of anhydrous tin(II) chloride (Alfa Aesar). After the salts were dissolved, 14.3 mg of Vulcan XC-72 carbon powder was added to the solution. The solution was sonicated for 10 min with intermittent stirring, followed by the immediate addition of 2 mL of freshly prepared 0.15 M sodium borohydride solution under rapid stirring. After 10 min, the solid carbon-supported catalysts were isolated by vacuum filtration with a poly(ether sulfone) (PES) membrane (Millipore Express PLUS Membrane Filter, 0.22 μm pore size, hydrophilic poly(ether sulfone)) and rinsed with ∼20 mL of DI water to remove excess borohydride and chloride salts. The membrane was removed from the filter and dried in air overnight until no moisture was visible on the membrane. The catalyst was gently scraped from the membrane and weighed. Depending on the final yield, the synthesis was repeated or scaled up to obtain enough product for testing in the fuel cell. PtRu/C, in 30 and 60 wt %, was purchased from the Fuel Cell Store and mixed in the appropriate ratio to yield an average loading of 53.3 wt % (8.5 mol %) to match the mole percent loading of the other catalysts (1.14 mg of 30 wt % + 3.99 mg of 60 wt %). For the Pt/C anode, 6 mg of catalyst powder was added to a vial with 1.5 mL of 1-propanol and 75 μL of quaternary ammonium poly(*N*-methylpiperidine-*co*-*p*-terphenyl) (QAPPT) ionomer (2 wt % in DMSO) and sonicated for 10 min with intermittent stirring. The entire ink was then sprayed onto a QAPPT anion exchange membrane (AEM) using an airbrush attached to a 3D printer (see the Supporting Information for details). The device was programmed to deposit the ink in a square shape with an edge length of 1.25 cm. This face of the membrane was used as the anode, while the reverse face was used as the cathode. The cathode was always deposited in the same manner with an ink that consisted of 6 mg of 60 wt % Pt/Ketjen black EC-300J (Fuel Cell Store) and 75 μL of QAPPT ionomer in 1.5 mL of 1-propanol. After the anode and cathode were sprayed, the MEA was soaked in 0.1 M KOH for at 70 °C for 16 h. The MEA was then removed and soaked in Nanopure water for 5 min before being placed in the fuel cell (Scribner 850 fuel cell test station and back pressure regulator). The cell fixture had a 5 cm^2, serpentine flow field on the anode and cathode sides and used Sigracet 28 BC gas diffusion electrodes (GDLs) on each side. The gas diffusion electrodes were cut into 1 × 1 cm squares and Teflon gaskets (McMaster-Carr, 0.005 in. thick) were cut to have a 1 × 1 cm square hole that created a tight fit around the GDLs. Pure hydrogen and oxygen were passed through humidifier tanks at 80 °C at a flow rate of 0.25 L/min before entering the fuel cell chambers, which were also held at 80 °C. The back pressure in the cell was held at 172 kPa gauge pressure (25 psi). The polarization curves were measured by increasing the current in steps of ∼8% of the total current until the maximum step size of 30 mA was reached. Then a step size of 30 mA was used until the cell voltage dropped to 0.3 V, which was followed by a faster return scan back to zero current (open circuit voltage) with a step size of 50 mA. The catalyst loading on the membrane was calculated by using a standardized procedure to account for the loss of material during the spraying process. The process was calibrated by spraying the catalyst ink several times onto aluminum foil and weighing on a microbalance after each deposition to calculate the percentage of the starting material that was deposited onto the substrate each time.

Scanning transmission electron microscopy (STEM) was used to image each catalyst and measure the particle sizes and *d*-spacings between crystal planes, as shown in Figure 3. Energy dispersive X-ray spectroscopy (EDS) was also used to spatially visualize the metallic elements in each catalyst at the subnanometer length scale. The samples were prepared for imaging by first dispersing them in ethanol by sonication and then placing a drop of the suspension onto a lacy carbon grid. The grid was dried in air at room temperature and then cleaned with an oxygen−argon plasma for 30 s before being placed in the microscope. STEM images were taken on an aberration-corrected ThermoFisher Scientific Spectra 300 X-CFEG electron microscope at 300 kV and 60 kV with a probe convergence semiangle of 30 mrad and a beam current of 56 pA. The EDS elemental maps were extracted after principal component analysis (PCA) denoising and background subtraction.

Powder X-ray diffraction patterns were obtained using a Rigaku SmartLab SE fitted with a copper X-ray anode and Cu Kβ filter. Samples were mounted using a single crystal silicon plate to minimize any background diffraction. X-ray photoelectron spectroscopy (XPS) data were obtained using a Physical Electronics VersaProbe III equipped with a monochromatic Al Kα X-ray source ($h\nu$ = 1486.6 eV), and the data were processed using CasaXPS. Charge neutralization was performed using both low energy electrons (<5 eV) and argon ions. The analysis spot size was ∼200 μm in diameter. Scanning electron microscopy was perfromed using a Zeiss Supra 50VP with an in-lens detector. Corresponding EDS maps and spectra were measured with an Oxford Ultim Max EDS detector at 30 kV accelerating voltage. Samples for SEM and XPS were prepared using carbon tape to mount the dry catalysts to an aluminum stub.

Data Preparation and Machine Learning. A data set was compiled by combining the experimental screening data with descriptors for each element that were derived from various literature sources, as shown in Table S1. Several steps were taken to prepare the descriptors for machine learning as described in detail in the Supporting Information. Most notably, the features were linearly scaled to range from 0 to 1 using the equation shown in Figure S1. A polynomial feature space of degree 2 was generated from all the columns in the space excluding self-interaction terms (Figure S2). Three regression models were used to analyze the training set data: a

https://doi.org/10.1021/acssuschemeng.2c05170
ACS Sustainable Chem. Eng. XXXX, XXX, XXX−XXX

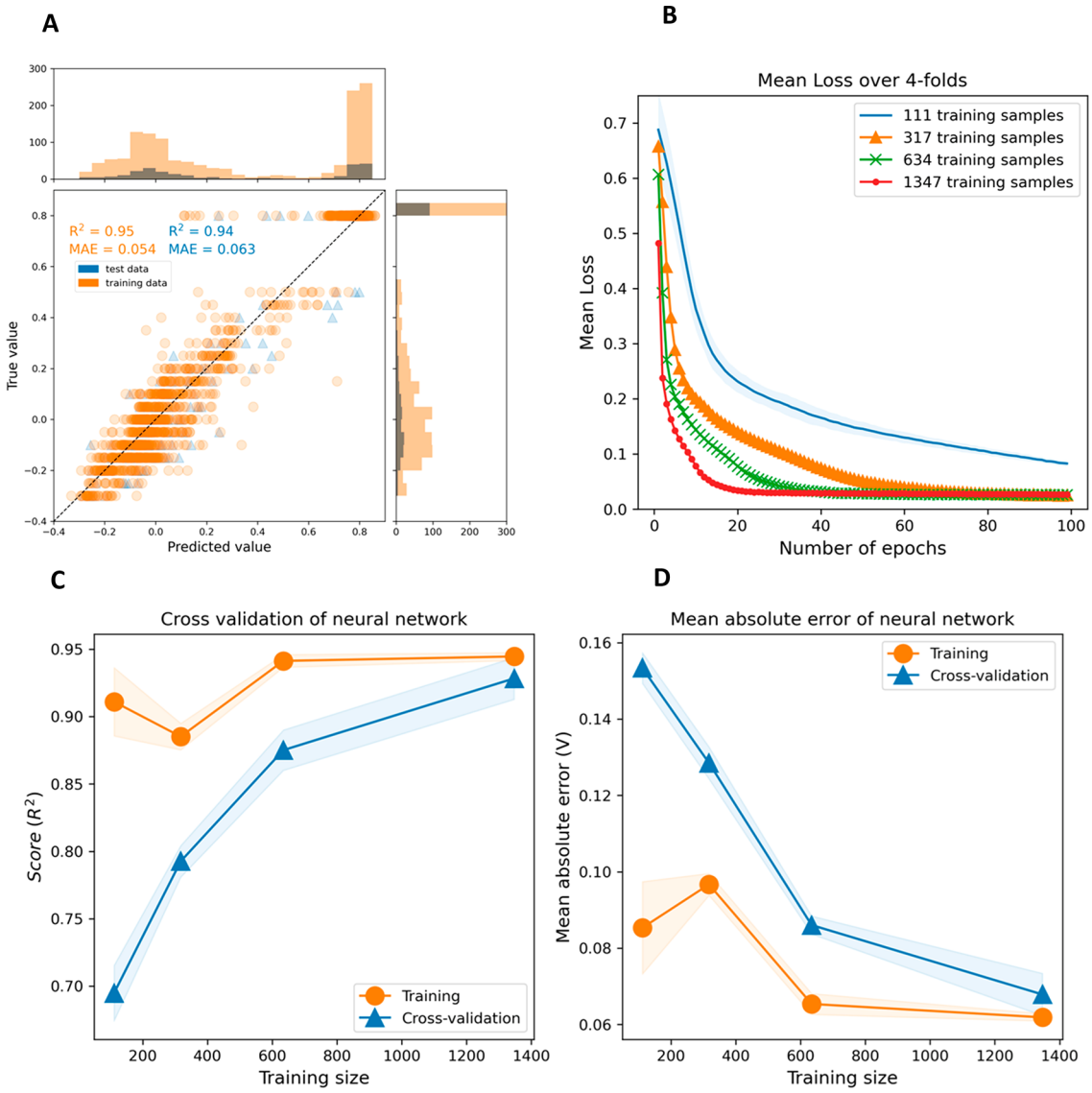

Figure 4. (A) Parity plot showing the accuracy of the neural network's predictions on the training data and test data after 1000 epochs. Histograms on each axis show the distribution of each axis data for qualitative comparison. (B) Plot of the average loss as a function of number of epochs during the training process. Four-fold cross-validation training showing model (C) accuracy and (D) mean absolute error after 400 epochs for each fold.

neural network (NN), a gradient boosted decision tree (GBDT),[41] and a Bayesian ridge model with automatic relevance determination (BRARD).[42] The results for each model are shown in Figures 4 and 5. The machine learning Python packages scikit-learn[43] and PyTorch[44] were used for data preprocessing, fitting, and evaluation. For the BRARD model, the optimization algorithm determines values of the weights, which can be used to determine which features are most significant for predicting the outcome. Similarly, for the GBDT model, we can calculate the significance of the features by using the Gini importance (normalized, mean decrease in accuracy).[45] Plots of the feature weights and their importance are shown in Figure 5B,E. Each model was also used to predict the onset voltage of the HOR for the test data, and the neural network was tested on a new array of alloys that was not in the training data. The accuracy of the training data and that of the test data for each model are summarized in parity plots in Figures 4A and 5A,D.

RESULTS AND DISCUSSION

High-throughput screening of alloy electrocatalysts was carried out with the use of a robotic liquid handler to prepare arrays and an optical screening method to measure the onset of electrocatalytic activity. Each array of 66 catalyst spots was fabricated on a common carbon working electrode by depositing precursor salts, and a chemical reductant was to create a ternary map of alloy compositions as shown in Figure 1C. The arrays were assembled into a custom screening cell shown in Figure 1A with a liquid electrolyte added to the top layer. The screening electrolyte contained a fluorescent, pH-sensitive probe molecule that images the generation of acid at the surface of active catalysts in the anodic HOR. As the potential on the array is stepped to progressively more anodic potentials, the most active spots in the array begin to fluoresce under UV flood illumination, and the fluorescence pattern is imaged by a digital camera. Each catalyst spot was separated by ~0.5 cm on the electrode, which is much greater than the diffusion length of ions during the 36 s potential step sequence; therefore, the pH gradient and resulting fluorescence gradient were well-resolved above the discrete catalyst spots as can be seen in Figure 1B. Twenty-four different arrays were

https://doi.org/10.1021/acssuschemeng.2c05170
ACS Sustainable Chem. Eng. XXXX, XXX, XXX−XXX

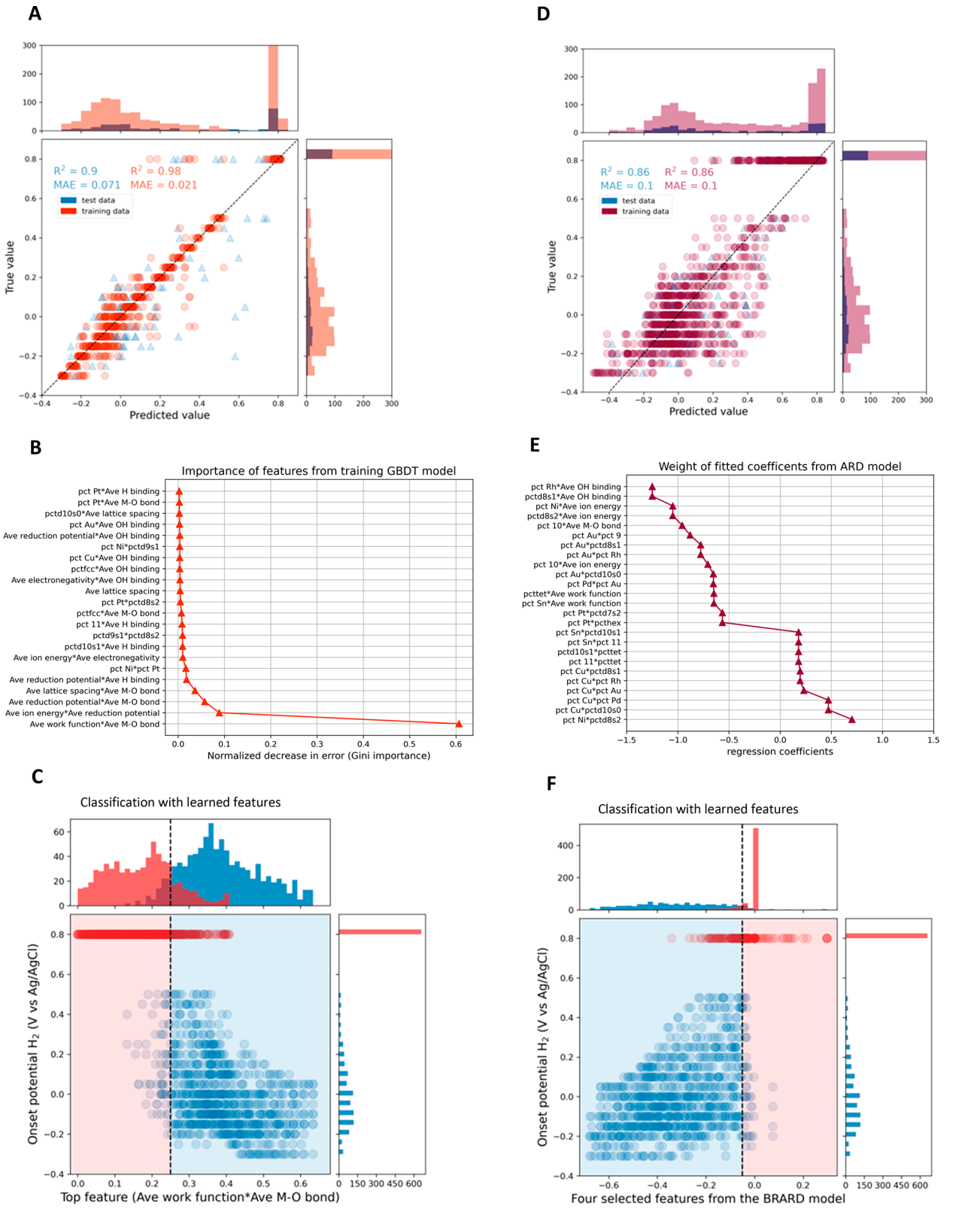

Figure 5. Parity plots showing the accuracy of the (A) GBDT and (D) BRARD linear regressor predictions for the training data and test data. Visualization of the feature importance of the top features from the (B) GBDT and (E) BRARD models. For the GBDT, feature importance is calculated using the normalized, total reduction of the mean squared error associated with each feature. For the BRARD model, the coefficients are the fitted regression coefficients. Plots to visualize the most significant features from each model versus the onset potential are shown for the (C) GBDT and (F) BRARD models. For the GBDT model, the features were Ave work function*Ave M−O bond enthalpy. For the BRARD model, the features were −(pct Rh*Ave OH adsorption) − (pct Ni*Ave ionization energy) − (pct 10*Ave M−O bond) + (pct Ni*pctd8s2). A clear separation can be seen between the alloys that are active and those that are not. A histogram projection and threshold line are plotted as a visual aid.

https://doi.org/10.1021/acssuschemeng.2c05170
ACS Sustainable Chem. Eng. XXXX, XXX, XXX−XXX

Table 1. Lattice Constants Measured from Lattice Fringes in STEM images and *d*-Spacings in XRD Patterns[a]

	lattice constant (Å)				
sample	from STEM	from XRD and std dev	from literature	crystallite size from XRD (nm)	electrochem surf.area (m^2/mol)
Pt/C	3.923 ± 0.112	3.918 ± 0.023	3.916[51]	5.66 ± 1.25	104.1
Pt_6Sn_4/C	3.862 ± 0.092	3.959 ± 0.016	3.959[51]	2.73 ± 0.41	121.7
Pt_2Rh_8/C	3.893 ± 0.095	3.881[b]	3.85[52,c]	1.76[b]	152.7
PtRu/C	3.907 ± 0.072	3.879 ± 0.020	3.875[53]	2.76 ± 0.23	103.3

[a]Values obtained from the STEM images have a low precision, which is likely caused by sample drift and nonuniform particle strain. [b]There is no standard deviation for this value because only one peak was observed by XRD. [c]This value was interpolated from literature data by using Vegard's law.

tested, each containing a combination of three elements chosen from a total group of 12 elements. These 12 elements were selected based on the solubility and stability of the precursor salts and the reducibility of the metal cation by sodium borohydride. The total number of ternary arrays that could be made from 12 elements was 12!/(9!3!) = 220, and the subset of these tested represents 11% of the total composition space. When selecting elements for the 12 arrays, we sought to create a uniform representation of the elements and binary combinations throughout the entire data set to minimize bias in the machine learning models. However, Ag was only combined with precursors that were available as nitrate salts to prevent precipitation of silver halides, and Hg was used in only one array because it did not adhere well to the carbon electrode. Only metallic compositions made by borohydride reduction were used in this study, but there is clearly potential for deliberately introducing main group elements such as nitrogen, boron, carbon, phosphorus, and sulfur in future experiments. The compositions of all the arrays that were screened can be seen in Figure S3.

On the basis of the screening results, two alloy compositions were chosen for more detailed investigation. We chose Pt_2Rh_8 because it had one of lowest anodic onset potentials of all the compositions tested, and we chose Pt_6Sn_4 because it also had a less anodic onset than Pt but contained significantly less precious metal. Rh/C catalysts have previously been reported to have similar activities for alkaline HOR to PtRu/C in rotating disk experiments, although the kinetics of both catalysts were too fast to differentiate the two.[46] PtSn/C alloys have previously been shown to be more active than Pt for methanol oxidation, but these catalysts have primarily been studied in acidic PEM fuel cells and the enhancement is generally attributed to weakening the CO* binding to Pt or to providing sites to adsorbed water.[47] In the case of the alkaline HOR, alloying with Sn may weaken the OH* adsorption energy at Pt or the presence of Sn^{4+} at the surface may modify the structure of adsorbed water. The two alloys were resynthesized to test their activities in an alkaline polymer fuel cell and to characterize their structures. The polarization curves in Figure 2 show that more power is produced by the Pt_6Sn_4 (132 mW/cm^2) and Pt_2Rh_8 (155 mW/cm^2) alloy anodes than pure Pt/C (103 mW/cm^2) but less power than commercial PtRu/C (202 mW/cm^2). The peak power and current observed in our tests also match closely with the average AEMFC metrics reported in the literature.[48] To quantify the role of surface area in the performances of these catalysts, the electrochemically active surface areas (ECSAs) were measured for each sample using the peak area from hydrogen underpotential deposition (H_{UPD}), and the values are reported in Table 1. The ECSA values measured fall into the expected range for Pt nanoparticles of this size,[49] although it has been shown that changes to the H* adsorption energy can affect the peak area of H_{UPD}.[50] We find that the ECSA does correlate with the peak power density for Pt/C, Pt_6Sn_4/C, and Pt_2Rh_8/C, but PtRu/C deviates strongly from this trend, which suggests that the superior performance of PtRu/C is not a result of higher ECSA. It has been shown previously that PtRu/C produces about twice as much power as Pt/C at the anode,[14] but the reason for improvement is still debated.[4]

Scanning transmission electron microscopy (STEM) was used to image the carbon-supported catalyst particles and to map the distribution of elements on the nanoscale. Figure 3 shows the electron micrographs with annotations for the crystal plane spacing as well as the elemental maps from EDS. The images show that the particle sizes for all the samples are similar to an average diameter of about 3 nm and a few polycrystalline particles that can be up to 7 nm in diameter. X-ray powder diffraction data (see below) indicated that nanoparticles of Pt/C, Pt_6Sn_4/C, and Pt_2Rh_8/C were face-centered cubic (fcc). Interplanar distances obtained from lattice fringes in the STEM images corresponded to the fcc (111) planes, and the calculated lattice constants are given in Table 1. The lattice constant for Pt is close to the value reported in the literature,[51] although the standard deviation for all the samples is high due to scan stability and nonuniform lattice strain. The STEM-derived lattice constants for Pt_6Sn_4, Pt_2Rh_8, and PtRu have large deviations from those previously reported in the literature,[51−53] but the lattice constants derived from the XRD patterns showed very close correspondence with the literature values and much smaller standard deviations. Energy dispersive X-ray spectroscopy (EDS) maps in Figure 3 show that the Pt_2Rh_8 and PtRu alloys have a homogeneous distribution of the elements throughout the particles, but Pt_6Sn_4 has a higher concentration of Sn in the 0.5 nm thick, outer shell of the particle (Figure 3D). A core−shell structure for PtSn alloys has been observed for similar samples and has also shown enhanced electrooxidation activity for ethanol, which the authors attributed to the favorable adsorption of OH* onto the SnO_2 surface.[54] It is unlikely that a pure SnO_2 surface would be very active for the HOR, suggesting that either there is some Pt/Sn alloying at the particle surface or the shell does not completely cover the Pt atoms at the surface.

Surface characterization of the alloys was done using X-ray photoelectron spectroscopy (XPS), and the measured spectra were fitted for surface quantification. The results are shown in Figures S4−S6 and summarized in Table 2. For the Pt_2Rh_8 and PtRu samples, the surface compositions are quite close to the target stoichiometries, and they are also close to the bulk compositions as measured by EDS. In contrast, XPS shows surface enrichment of Sn in the Pt_6Sn_4 sample, which is consistent with the STEM imaging results. On the basis of this information and the EDS maps, we believe that, in the PtRu

https://doi.org/10.1021/acssuschemeng.2c05170
ACS Sustainable Chem. Eng. XXXX, XXX, XXX−XXX

Table 2. Comparison of Target Stoichiometry, Bulk Composition as Measured by EDS, and Surface Composition as Measured by XPS

	Pt:Me atomic ratio (Me = Sn, Rh, Ru)		
sample	target stoichiometry	bulk composition (EDS)	surface composition (XPS)
Pt_2Rh_8	0.25	0.26	0.23
Pt_6Sn_4	1.50	1.38	1.26
PtRu	1.00	1.12	1.01

and Pt_2Rh_8 samples, Pt, Ru, and Rh are all exposed at the surface of the particles and thus can be catalytically active sites. The amount of Pt on the surface of the Pt_6Sn_4 sample is difficult to quantify because we know from EDS that only the top 0.5 nm is enriched in Sn. However, we measure a 56:44 Pt:Sn ratio by XPS. This suggests there is considerable platinum within 1−2 nm of the surface that could interact directly with H atoms. The EDS map in Figure 3D also shows brownish/orange-colored pixels on the surface of the Pt_6Sn_4 particle, which indicates that both Pt and Sn was detected at those locations on the surface. We observed by XPS that the Pt $4f_{7/2}$ peak was shifted by +0.5 eV in the more active alloys with Ru and Rh but not in the Sn alloy. This shift could be caused by three effects, i.e., the presence of PtO in the PtRu and Pt_2Rh_8 samples, a partial transfer of charge from the Pt atoms to the Ru or Rh atoms, or a particle size effect previously reported by Roth et al.[55] In addition, peak shifts have also been attributed to rehybridization of valence orbitals, volume renormalization, or changes to charge screening of core holes.[56] Several other studies of alloys have observed this shift in binding energy after taking careful steps to prevent or remove surface oxidation, supporting the idea that the peak shifts are caused by transfer of charge between the atoms or a particle size effect rather than by surface oxidation. Unfortunately, conflicting results are reported in the literature for the direction of the peak shifts in PtRu alloys which may be dependent on the sample preparation method or the other factors mentioned above. Most observations report a positive shift of +0.5 eV.[57,58] PtSn alloys typically exhibit a negative shift (−0.7 eV) of the Pt 4f peaks,[58,59] whereas PtRh alloys[60] were previously reported to have no shift of the Pt 4f peaks, both of which are contrary to our observations. All the atoms in the alloys have unfilled valence shells that could donate or accept electrons from neighboring atoms. Pt, Ru, and Rh have similar electronegativities and based on that consideration alone would not be expected to transfer charge locally between atoms, whereas Sn has a much lower electronegativity and would be expected to donate charge to Pt in an alloy. This expectation is however the exact opposite of our observation, as well as of most other observations of PtRu and PtSn alloys, and is an ongoing debate within the community.[61] Rodriguez et al. reported a significant correlation between the shift in core level electrons measured by XPS and the adsorption energy of carbon monoxide on the surface, which was attributed to a change in the valence d-band due to rehybridization, but it should be noted that other factors can affect the energy of core electrons.[56] Hammer and Nørskov[62,63] created the d-band model for heterogeneous catalysis, which has shown a strong correlation between catalytic activity and adsorbate stability.[64] A shift in the d-band could thus be correlated with activity depending on the direction and magnitude of the shift.[15] The ideal catalyst was predicted to have slightly weaker H* adsorption (+0.3 ΔeV) than Pt(111) and stronger OH* adsorption (−1.0 ΔeV) than Pt(111).[15] Since Pt_6Sn_4 did not have a noticeable shift in the Pt 4f peak, we hypothesize there may not be a shift in the d-band or adsorption energies and that a bifunctional mechanism could be the cause of increased HOR activity. Sn has one of the strongest OH* adsorption energies of the metals tested, and Koper et al. have previously used DFT calculations to show that stronger OH* adsorption would be beneficial for catalysis of the alkaline hydrogen evolution reaction (HER) and likely also for the HOR.[15] Since PtRu and Pt_2Rh_8 both showed a binding energy shift in the Pt core electrons, it is possible that a shift in the d-band contributed to improved activity. However, we cannot rule out the other factors noted above that affect this measurement.

Peak fitting of the XPS data suggests that all the alloying metals, Rh, Ru and Sn, on the surface of the catalyst particles are predominantly oxidized. Previous studies of PtRu/C also found that the surface Ru atoms were mostly oxidized to Ru(IV) and Ru(V), especially when the water content was high in the synthesis.[65,66] Likewise, PtSn and PtRh alloys have been shown to have oxidized surfaces via XPS, although this this may depend on the conditions of the synthesis and exposure to air in preparation for ex situ measurements.[67−69]

Powder X-ray diffraction (XRD) patterns in Figures S7−S10 of the catalysts tested confirmed that only one crystalline fcc phase was detected in each sample. Interestingly, the Pt_2Rh_8 alloy showed only a single, broad peak centered near the expected 2θ value of the (111) peak of Pt and Rh, which has previously been seen for alloys with high Rh content,[52,70] and this suggests that the sample contains particles with a broad ensemble of lattice constants. There is obvious peak shifting for Pt_6Sn_4 and PtRu compared to pure Pt. The Pt_6Sn_4 peaks are shifted to lower 2θ angles by ∼0.25°, whereas the PtRu peaks are shifted to higher angles by ∼1°. Lattice constants calculated from the *d*-spacings of the (111) peaks and are compared in Table 1 to those derived from STEM images and earlier literature reports. The shift of the diffraction peaks suggests that alloying may contribute to lattice strain. Previous studies by Du et al. have shown that mechanically induced compressive strain in a pure Pt film increases its activity for oxygen reduction whereas tensile strain lowers its activity.[50] It has been shown that the increase in the oxygen reduction reaction (ORR) activity on Pt is due to weakening of O* adsorption which moves it toward the optimal adsorption strength.[71] This may not be the case for OH* or H*, and alloy surfaces complicate the understanding of strain effects because it is not clear what the active sites are. From our knowledge of the activity of the pure elements, we hypothesize that Rh and Pt are likely both active sites for binding the intermediates because of their high activities for alkaline HOR. Ru also has moderate activity for alkaline HOR, but it is not possible to determine which element in the alloys the intermediates are adsorbed to or how strongly without more experimental or computational data. We note that studies have shown evidence that OH* adsorbs to Ru sites and H* adsorbs to Pt sites in a Pt_3Ru alloy.[14] From the XRD data, we observed that Pt_2Rh_8 and PtRu had lattice compressions of 2.1 and 1.0% relative to pure Pt, whereas Pt_6Sn_4 had a lattice expansion of 1.0%. This indicates that the higher HOR activity of Pt_6Sn_4 does not correlate with lattice strain, and thus a bifunctional mechanism may be operative as suggested by the lack of an XPS peak shift. It is not clear if the higher activities of PtRu and Pt_2Rh_8 are due to compressive strain or electronic effects since the degree of

https://doi.org/10.1021/acssuschemeng.2c05170
ACS Sustainable Chem. Eng. XXXX, XXX, XXX−XXX

strain is lower in the more active PtRu catalyst. Pt_6Sn_4 and PtRu appear to have some preferred orientation as evidenced by the low intensity of the (200) peak, which is often seen in Pt alloys with these elements.[52,53,72] We also calculated the average crystallite size of the particles by using the Scherrer equation. This indicated that the average Pt crystalline domain size was about 5.7 nm, and that PtRu and Pt_6Sn_4 had average sizes of 2.7 nm, which agrees well with the observations from STEM images and ECSA measurements. The (111) peak for Pt_2Rh_8 gave an average crystallite size of 1.8 nm, but it is not clear if the increased peak width was primarily a consequence of particle size or the presence of overlapping reflections from grains with different *d*-spacings.

The catalyst screening data were prepared for machine learning as described in the Supporting Information. The sample set used for training and testing is represented as a graph network in Figure 1D to visualize how homogeneously the elements are represented in the data set. Mercury was used in only one array due to its lack of activity for HOR and poor adhesion to the electrode. Silver was used only with metals that were available as nitrate salts in order to avoid the formation of insoluble silver chloride. The data set was designed to include as many unique binary combinations as possible while following those two constraints.

The experimental screening data were used to train three different regression models: a neural network (NN), a gradient boosted decision tree (GBDT),[41] and a Bayesian ridge model with automatic relevance determination (BRARD).[42] Today, it is common for machine learning models to be trained on several hundred thousand data points, which can be an impractically large number for analyses based on experimental data. Thus, a key goal of the current study was to determine whether more sparse data sets could enable accurate predictions of electrocatalytic activity. The accuracy of all three models is high when interpolating the onset potential of catalysts, considering the small size of the training data set.

The NN model was chosen for study in more detail because it exhibited both the highest test accuracy and minimal overfitting. The accuracy of the NN can be summarized by examining the parity plot in Figure 4A. The coefficient of determination (R^2) has values of 0.95 and 0.94 for the training and test sets, respectively, while the mean absolute errors (MAEs) for HOR onset potentials are 0.054 and 0.063 V. A perfect model would have all data points fall directly on the parity line and have an R^2 of 1 and MAE of 0. Figure 4B shows that the NN's loss during each training loop (described as an epoch) decreases rapidly and converges very quickly. Four-fold cross validation was performed during training of the NN to calculate a less biased score and check for overfitting. We also experimented with using different training sizes to visualize how adding more data points could affect the test accuracy. From Figure 4C,D, we see that test accuracy and mean error improve rapidly with the training sample size up to ~350 samples, after which they change more slowly. Thus, while the model could likely be improved with more data, the test accuracy is improving slowly, and the training accuracy has already reached a plateau with the current data set. We also note that the large difference in training accuracy and test accuracy seen for the smallest training size in Figure 4C,D is a result of the network being too large for the small data set and overfitting, although this difference diminishes as the training data size grows to fit the network size.

The parity plots and test metrics for the GBDT and BRARD models are shown in Figure 5A,D. Using these metrics, we can see that the NN and GBDT perform very similarly on the training and testing data while the BRARD model performs more poorly in both cases. To predict the onset potential of an entirely new array that is not included in the training data, we retrained the NN without the data of the SnPtRh array and used it to predict the onset potentials of the SnPtRh array. The predicted and experimental onset potentials for alkaline HOR are shown in Figure 2B,C. R^2 decreased dramatically to 0.034 but the MAE only increased to 0.12 (Figure S11). which is similar to the value obtained from the ridge regression model (0.1 V) and only 2 times the best values obtained from the other models. This shows that the predictions for SnPtRh are actually not so far off from the true values. The reason why the R^2 value is so low for this data set is because 89% of the data from just this one array (SnPtRh) falls within the range of the mean error. The average onset potential is around 0.05 V but the average error is ±0.12 V, and 89% of the data falls within this range of the mean. In other words, experimental error, random error, and other sources of error can cause a deviation up to 0.12 V but 89% of the data falls within this small window of fluctuations. Therefore, the reason the R^2 value is so low is not because the model is not accurate, but rather because this data set has such a narrow range of onset potentials compared to the magnitude of the error. However, we want to emphasize that having a narrow range of onset potentials for this data does not make the predictions useless as we can see the average error is only 0.12 V, and it is obvious that the few data points that are far from the mean do seem to follow the diagonal line though there are so few that it cannot affect the statistical significance of the R^2 value. With a comparison of the onset potentials of binary compositions that are repeated across different arrays, a deviation in onset potentials as large as 0.1 V can be found in a few instances, which is likely due to deviations in the robotic synthesis and/or drift of the Ag/AgCl reference electrode. Another major source of error comes from estimating the intrinsic material properties of the alloys by taking a simple weighted average of the properties of the individual component elements. This is clearly inaccurate in many cases and could be improved by incorporating descriptors for alloy phase behavior, by high-throughput characterization experiments of the alloys, or by applying advanced computational chemistry/physics models to calculate the alloy properties. This model could be used to predict the HOR activity of any binary or ternary alloy containing the 12 elements used in the screening and could also be adapted to include any element by adding the relevant physical properties of each element into the model database.

To better understand the factors that determine the activity of the catalysts, we plot the normalized, mean decrease in the mean squared error for the top 22 features after training the GBDT model in Figure 5B. Since these decision trees use inequalities for the splitting criteria, we would expect good predictor features to be separated by some threshold value as shown in Figure 5C. By far the most significant feature is the product of the average work function and the average metal oxide bond enthalpy. The M−O bond enthalpy is highest for Sn, Rh, Pt, Co, and Fe while Pt, Pd, Au, and Ni have the highest work functions. The product of these two properties would therefore enhance the contribution of Pt relative to those of Co, Fe, and Au. Next, we see two more features, which contain products of the reduction potential with metal oxide

https://doi.org/10.1021/acssuschemeng.2c05170
ACS Sustainable Chem. Eng. XXXX, XXX, XXX−XXX

bond enthalpy and ionization energy. We see that features related to the amounts of Pt (pct Pt, pctd9s1) and Ni (pct Ni, pctd8s2) play a small role in determining the prediction for the GBDT model as well as the adsorption energies of H* and OH*, though they are much less significant to the model than the main features mentioned earlier. It should also be noted that pct Pt and pct Ni are both perfectly correlated to pctd9s1 and pctd8s2, so the total contribution of these features should be considered together. The low ranking for H* and OH* adsorption energies from this model does not mean that these features are not important for the activity, but rather that they are not the best descriptors when considering the entire range of metals tested. Adsorption energy would likely be more significant if we were only considering the most catalytically active metals in this study. Also, particle size clearly plays an important role in the ranking of catalytic activity, as shown by the ECSA measurements. Thus, the relative rates of nanoparticle nucleation and growth are expected to be important and may correlate with some of the elemental features identified by the NN and GBDT models.

Plots of the most significant coefficients from the BRARD model are shown in Figure 5E, and we would expect to see a strong correlation between these features and the onset potential shown in Figure 5F. The use of a polynomial feature space is quite useful here because it enables the model to accurately fit a combination of parabolic relationships that may exist between a positively correlated feature and a negatively correlated feature (Figure S2). We can see large a positive coefficient associated with Ni content (pct Ni*pctd8s2), which pushes the onset potential higher as the value increases. We also see that products of elemental content (pct Cu times pct Rh, pct Au, and pct Pd) have large, positive coefficients which again push the onset potential higher when there is high Cu content in the sample with Rh, Au, or Pd. These features suggest that Cu may have a detrimental effect on the activity of active metals, Pd and Rh, which supports our observations from the arrays containing Cu and Pd or Rh in Figure S12. Notably, we do not see combinations of Pt and Cu in this list of bad features, which again supports the observation in Figure S12. Next, we observe high, negative coefficients associated with Rh content (pct Rh and pctd8s1) times the average OH* adsorption energy as well as the ionization energy times Ni content (pctd8s2 and pct Ni). This suggests that Rh should be more active when alloyed with metals that have a lower OH* adsorption energy, such as Fe, Co, or Sn, which is supported by our observations in Figure S12. Seeing the presence of pct Ni and pctd8s2 show up in both the positive and negative weights is a consequence of a model that uses a sum of the features to balance the complex relationship between the alloy's activity and composition. In Figure 5C,F we show scatter plots between the onset potential and the top features as well as the projections onto each axis. By looking at the projection onto the x-axis and separating the data into two classes, active and inactive, we can visually identify where the optimal value lies for a catalyst without having to use the machine learning model to predict the onset potential and with only needing to know a few attributes of the sample. This can be used as a simple classifier to predict if an alloy will fall into the class of active or inactive. Using this method of classification with the top feature from the GBDT shown in Figure 5C, we observe a correct prediction for 89% of the data while the classification with four selected features from the BRARD model shown in Figure 5E is correct 92% of the time. It is not surprising that the classification that used the features from the BRARD model performed better than the classification from the GBDT model because BRARD is optimized to fit a linear combination of features and this classification method uses a linear combination of the top features. This shortcut would only be accurate for catalysts that are similar to those that were used in this study, mainly late row transition metal and p-block metal alloys.

CONCLUSIONS

A goal of this study was to understand the predictive power of machine learning tools with a limited experimental data set of electrocatalyst onset potentials. In this context, the high accuracies of interpolation by the NN and GBDT models are encouraging and suggest that they could be useful for predicting new, active catalysts if the quality of training data can be improved and extended. The accuracy of interpolation suggests that meaningful predictions about catalysis can be made with only a few thousand data points if enough information can be incorporated into the model, in contrast to other studies that have used up to 2 orders of magnitude more data points.[30] It is well-known that machine learning models perform worse at extrapolating beyond the boundaries of the training data, and this may be improved by expanding the elemental boundaries or by using physics-informed or expert-in-the-loop models.[73] The incorporation of metals such as Ru and Ir would likely lead to more active catalysts,[13] and metals such as Mo and Mn may also show interesting activity if they can be stabilized in nanoparticle alloys. It is likely that the accuracy of the models used for extrapolation could be improved significantly by gathering more accurate data from the alloys or by improving the precision of the screening method. Regardless, these experiments have shown that we can give a reasonably accurate estimate of an alloy catalyst's HOR activity just by looking at the average metal−oxygen bond enthalpy times the average work function of the individual elements, and using the trained NN, one can quickly and accurately estimate the onset potential of an alloy HOR catalyst.

ASSOCIATED CONTENT

Supporting Information

The Supporting Information is available free of charge at https://pubs.acs.org/doi/10.1021/acssuschemeng.2c05170.

Experimental details of electrochemical screening, MEA fabrication, fuel cell testing, materials characterization, and image analysis, XPS, X-ray powder diffraction, cyclic voltammetry, EDS, SEM, and STEM images of electrocatalysts; computational details, graph network of elements, database used for alloy samples, illustration of polynomial features that create a nonlinear basis set, visualization of the data set used for training and testing of machine learning models, parity plot and measured onset potentials of electrocatalysts, and complete data set used for machine learning (PDF)

AUTHOR INFORMATION

Corresponding Author

Thomas E. Mallouk − *Department of Chemistry, The University of Pennsylvania, Philadelphia, Pennsylvania 19104, United States;* orcid.org/0000-0003-4599-4208; Email: mallouk@sas.upenn.edu

https://doi.org/10.1021/acssuschemeng.2c05170
ACS Sustainable Chem. Eng. XXXX, XXX, XXX−XXX

Authors

Jeremy L. Hitt − *Department of Chemistry, The University of Pennsylvania, Philadelphia, Pennsylvania 19104, United States*

Dasol Yoon − *Department of Materials Science and Engineering, Cornell University, Ithaca, New York 14853, United States;* orcid.org/0000-0003-2284-7010

Jeffrey R. Shallenberger − *Materials Research Institute, Pennsylvania State University, University Park, Pennsylvania 16802, United States*

David A. Muller − *School of Applied and Engineering Physics, Cornell University, Ithaca, New York 14853, United States; Kavli Institute at Cornell for Nanoscale Science, Ithaca, New York 14853, United States*

Complete contact information is available at: https://pubs.acs.org/10.1021/acssuschemeng.2c05170

Author Contributions

T.E.M. and D.A.M. supervised the project. J.L.H. planned and executed the electrochemical screening experiments, MEA fabrication, fuel cell testing, data processing, and machine learning. J.L.H. also performed the SEM and XRD characterization. D.Y. performed the TEM/EDS imaging, and J.R.S. acquired and analyzed the XPS data. All authors contributed to the writing of the manuscript.

Notes

The authors declare no competing financial interest.

■ ACKNOWLEDGMENTS

This work was performed as part of the Center for Alkaline-Based Energy Solutions (CABES), an Energy Frontier Research Center funded by the U.S. Department of Energy, Office of Science, Basic Energy Sciences, under Award DE-SC0019445. J.L.H. acknowledges support as a graduate fellow of the Vagelos Institute for Energy Science and Technology at the University of Pennsylvania, and T.E.M. and J.L.H. also acknowledge support from the Canadian Institute for Advanced Research (CIFAR). This work made use of TEM facilities at the Cornell Center for Materials Research (CCMR) which are supported through the National Science Foundation Materials Research Science and Engineering Center (NSF MRSEC) program (DMR-1719875). The ThermoFisher Spectra 300 X-CFEG was supported through PARADIM, an NSF Materials Innovation Platform (DMR-2039380), and Cornell University. SEM analyses were performed using instruments in the Materials Characterization Core at Drexel University. Instrumentation and facilities used in this project were supported, in part, by the Materials Characterization Lab of the Penn State Materials Research Institute (MRI). We thank Zhifei Yan and Yuguang (Chris) Li for their contributions in testing and troubleshooting experiments and for helpful discussions. J.L.H. and T.E.M also acknowledge support from the University of Pennsylvania and the Vagelos Institute for Energy Science and Technology.

■ REFERENCES

(1) *Renewable Power Generation Costs in 2017*. https://www.irena.org/publications/2018/Jan/Renewable-power-generation-costs-in-2017 (accessed 2022-04-02).

(2) Dowling, J. A.; Rinaldi, K. Z.; Ruggles, T. H.; Davis, S. J.; Yuan, M.; Tong, F.; Lewis, N. S.; Caldeira, K. Role of Long-Duration Energy Storage in Variable Renewable Electricity Systems. *Joule* **2020**, *4* (9), 1907−1928.

(3) Bullock, M.; More, K. *Basic Energy Sciences Roundtable: Foundational Science for Carbon-Neutral Hydrogen Technologies (Report)*; DOESC Office of Basic Energy Sciences: 2022. DOI: 10.2172/1834317.

(4) Yang, Y.; Peltier, C. R.; Zeng, R.; Schimmenti, R.; Li, Q.; Huang, X.; Yan, Z.; Potsi, G.; Selhorst, R.; Lu, X.; Xu, W.; Tader, M.; Soudackov, A. V.; Zhang, H.; Krumov, M.; Murray, E.; Xu, P.; Hitt, J.; Xu, L.; Ko, H.-Y.; Ernst, B. G.; Bundschu, C.; Luo, A.; Markovich, D.; Hu, M.; He, C.; Wang, H.; Fang, J.; DiStasio, R. A.; Kourkoutis, L. F.; Singer, A.; Noonan, K. J. T.; Xiao, L.; Zhuang, L.; Pivovar, B. S.; Zelenay, P.; Herrero, E.; Feliu, J. M.; Suntivich, J.; Giannelis, E. P.; Hammes-Schiffer, S.; Arias, T.; Mavrikakis, M.; Mallouk, T. E.; Brock, J. D.; Muller, D. A.; DiSalvo, F. J.; Coates, G. W.; Abruña, H. D. Electrocatalysis in Alkaline Media and Alkaline Membrane-Based Energy Technologies. *Chem. Rev.* **2022**, *122* (6), 6117−6321.

(5) Wang, Y.; Yang, Y.; Jia, S.; Wang, X.; Lyu, K.; Peng, Y.; Zheng, H.; Wei, X.; Ren, H.; Xiao, L.; Wang, J.; Muller, D. A.; Abruña, H. D.; Hwang, B. J.; Lu, J.; Zhuang, L. Synergistic Mn-Co Catalyst Outperforms Pt on High-Rate Oxygen Reduction for Alkaline Polymer Electrolyte Fuel Cells. *Nat. Commun.* **2019**, *10* (1), 1506.

(6) Xie, X.; He, C.; Li, B.; He, Y.; Cullen, D. A.; Wegener, E. C.; Kropf, A. J.; Martinez, U.; Cheng, Y.; Engelhard, M. H.; Bowden, M. E.; Song, M.; Lemmon, T.; Li, X. S.; Nie, Z.; Liu, J.; Myers, D. J.; Zelenay, P.; Wang, G.; Wu, G.; Ramani, V.; Shao, Y. Performance Enhancement and Degradation Mechanism Identification of a Single-Atom Co−N−C Catalyst for Proton Exchange Membrane Fuel Cells. *Nat. Catal.* **2020**, *3* (12), 1044−1054.

(7) Martinez, U.; Komini Babu, S.; Holby, E. F.; Chung, H. T.; Yin, X.; Zelenay, P. Fe−N−C Catalysts: Progress in the Development of Fe-Based PGM-Free Electrocatalysts for the Oxygen Reduction Reaction (Adv. Mater. 31/2019). *Adv. Mater.* **2019**, *31* (31), 1970224.

(8) Zhang, H. T.; Chung, H. A.; Cullen, D.; Wagner, S. I.; Kramm, U. L.; More, K.; Zelenay, P.; Wu, G. High-Performance Fuel Cell Cathodes Exclusively Containing Atomically Dispersed Iron Active Sites. *Energy Environ. Sci.* **2019**, *12* (8), 2548−2558.

(9) Sheng, W.; Gasteiger, H. A.; Shao-Horn, Y. Hydrogen Oxidation and Evolution Reaction Kinetics on Platinum: Acid vs Alkaline Electrolytes. *J. Electrochem. Soc.* **2010**, *157* (11), B1529.

(10) Durst, J.; Siebel, A.; Simon, C.; Hasché, F.; Herranz, J.; Gasteiger, H. A. New Insights into the Electrochemical Hydrogen Oxidation and Evolution Reaction Mechanism. *Energy Environ. Sci.* **2014**, *7* (7), 2255−2260.

(11) Sheng, W.; Zhuang, Z.; Gao, M.; Zheng, J.; Chen, J. G.; Yan, Y. Correlating Hydrogen Oxidation and Evolution Activity on Platinum at Different PH with Measured Hydrogen Binding Energy. *Nat. Commun.* **2015**, *6* (1), 1−6.

(12) Nørskov, J. K.; Bligaard, T.; Logadottir, A.; Kitchin, J. R.; Chen, J. G.; Pandelov, S.; Stimming, U. Trends in the Exchange Current for Hydrogen Evolution. *J. Electrochem. Soc.* **2005**, *152* (3), J23−J26.

(13) Strmcnik, D.; Uchimura, M.; Wang, C.; Subbaraman, R.; Danilovic, N.; van der Vliet, D.; Paulikas, A. P.; Stamenkovic, V. R.; Markovic, N. M. Improving the Hydrogen Oxidation Reaction Rate by Promotion of Hydroxyl Adsorption. *Nat. Chem.* **2013**, *5* (4), 300−306.

(14) Wang, Y.; Wang, G.; Li, G.; Huang, B.; Pan, J.; Liu, Q.; Han, J.; Xiao, L.; Lu, J.; Zhuang, L. Pt−Ru Catalyzed Hydrogen Oxidation in Alkaline Media: Oxophilic Effect or Electronic Effect? *Energy Environ. Sci.* **2015**, *8* (1), 177−181.

(15) McCrum, I. T.; Koper, M. T. M. The Role of Adsorbed Hydroxide in Hydrogen Evolution Reaction Kinetics on Modified Platinum. *Nat. Energy* **2020**, *5* (11), 891−899.

(16) Zhu, S.; Qin, X.; Yao, Y.; Shao, M. PH-Dependent Hydrogen and Water Binding Energies on Platinum Surfaces as Directly Probed through Surface-Enhanced Infrared Absorption Spectroscopy. *J. Am. Chem. Soc.* **2020**, *142* (19), 8748−8754.

(17) Cheng, T.; Wang, L.; Merinov, B. V.; Goddard, W. A. Explanation of Dramatic pH-Dependence of Hydrogen Binding on

Noble Metal Electrode: Greatly Weakened Water Adsorption at High PH. *J. Am. Chem. Soc.* **2018**, *140* (25), 7787−7790.
(18) Ramaswamy, N.; Ghoshal, S.; Bates, M. K.; Jia, Q.; Li, J.; Mukerjee, S. Hydrogen Oxidation Reaction in Alkaline Media: Relationship between Electrocatalysis and Electrochemical Double-Layer Structure. *Nano Energy* **2017**, *41*, 765−771.
(19) Weber, D. J.; Janssen, M.; Oezaslan, M. Effect of Monovalent Cations on the HOR/HER Activity for Pt in Alkaline Environment. *J. Electrochem. Soc.* **2019**, *166* (2), F66.
(20) Sarabia, F. J.; Sebastián-Pascual, P.; Koper, M. T. M.; Climent, V.; Feliu, J. M. Effect of the Interfacial Water Structure on the Hydrogen Evolution Reaction on Pt(111) Modified with Different Nickel Hydroxide Coverages in Alkaline Media. *ACS Appl. Mater. Interfaces* **2019**, *11* (1), 613−623.
(21) Okubo, K.; Ohyama, J.; Satsuma, A. Surface Modification of Pt Nanoparticles with Other Metals Boosting the Alkaline Hydrogen Oxidation Reaction. *Chem. Commun.* **2019**, *55* (21), 3101−3104.
(22) Scofield, M. E.; Zhou, Y.; Yue, S.; Wang, L.; Su, D.; Tong, X.; Vukmirovic, M. B.; Adzic, R. R.; Wong, S. S. Role of Chemical Composition in the Enhanced Catalytic Activity of Pt-Based Alloyed Ultrathin Nanowires for the Hydrogen Oxidation Reaction under Alkaline Conditions. *ACS Catal.* **2016**, *6* (6), 3895−3908.
(23) Cong, Y.; McCrum, I. T.; Gao, X.; Lv, Y.; Miao, S.; Shao, Z.; Yi, B.; Yu, H.; Janik, M. J.; Song, Y. Uniform $Pd_{0.33}Ir_{0.67}$ Nanoparticles Supported on Nitrogen-Doped Carbon with Remarkable Activity toward the Alkaline Hydrogen Oxidation Reaction. *J. Mater. Chem. A* **2019**, *7* (7), 3161−3169.
(24) Jervis, R.; Mansor, N.; Gibbs, C.; Murray, C. A.; Tang, C. C.; Shearing, P. R.; Brett, D. J. L. Hydrogen Oxidation on PdIr/C Catalysts in Alkaline Media. *J. Electrochem. Soc.* **2014**, *161* (4), F458.
(25) Wang, H.; Abruña, H. D. Rh and Rh Alloy Nanoparticles as Highly Active H_2 Oxidation Catalysts for Alkaline Fuel Cells. *ACS Catal.* **2019**, *9* (6), 5057−5062.
(26) Miller, H. A.; Lavacchi, A.; Vizza, F.; Marelli, M.; Di Benedetto, F.; D'Acapito, F.; Paska, Y.; Page, M.; Dekel, D. R. A Pd/C-CeO_2 Anode Catalyst for High-Performance Platinum-Free Anion Exchange Membrane Fuel Cells. *Angew. Chem., Int. Ed.* **2016**, *55* (20), 6004−6007.
(27) Yu, H.; Davydova, E. S.; Ash, U.; Miller, H. A.; Bonville, L.; Dekel, D. R.; Maric, R. Palladium-Ceria Nanocatalyst for Hydrogen Oxidation in Alkaline Media: Optimization of the Pd−CeO_2 Interface. *Nano Energy* **2019**, *57*, 820−826.
(28) Reddington, E.; Sapienza, A.; Gurau, B.; Viswanathan, R.; Sarangapani, S.; Smotkin, E. S.; Mallouk, T. E. Combinatorial Electrochemistry: A Highly Parallel, Optical Screening Method for Discovery of Better Electrocatalysts. *Science* **1998**, *280* (5370), 1735−1737.
(29) Reddington, E.; Yu, J.-S.; Sapienza, A.; Chan, B. C.; Gurau, B.; Viswanathan, R.; Liu, R.; Smotkin, E. S.; Sarangapani, S.; Mallouk, T. E. Combinatorial Screening of Anode and Cathode Electrocatalysts for Direct Methanol Fuel Cells. *MRS Online Proceedings Library* **1998**, *549* (1), 231−236.
(30) Yang, L.; Haber, J. A.; Armstrong, Z.; Yang, S. J.; Kan, K.; Zhou, L.; Richter, M. H.; Roat, C.; Wagner, N.; Coram, M.; Berndl, M.; Riley, P.; Gregoire, J. M. Discovery of Complex Oxides via Automated Experiments and Data Science. *Proc. Natl. Acad. Sci. U. S. A.* **2021**, *118* (37), No. e2106042118.
(31) Xiang, C.; Suram, S. K.; Haber, J. A.; Guevarra, D. W.; Soedarmadji, E.; Jin, J.; Gregoire, J. M. High-Throughput Bubble Screening Method for Combinatorial Discovery of Electrocatalysts for Water Splitting. *ACS Comb. Sci.* **2014**, *16* (2), 47−52.
(32) Gregoire, J. M.; Xiang, C.; Liu, X.; Marcin, M.; Jin, J. Scanning Droplet Cell for High Throughput Electrochemical and Photoelectrochemical Measurements. *Rev.f Sci. Inst.* **2013**, *84* (2), 024102.
(33) Hitt, J. L.; Li, Y. C.; Tao, S.; Yan, Z.; Gao, Y.; Billinge, S. J. L.; Mallouk, T. E. A High Throughput Optical Method for Studying Compositional Effects in Electrocatalysts for CO_2 Reduction. *Nat. Commun.* **2021**, *12* (1), 1114.
(34) Shinde, A.; Jones, R. J. R.; Guevarra, D.; Mitrovic, S.; Becerra-Stasiewicz, N.; Haber, J. A.; Jin, J.; Gregoire, J. M. High-Throughput Screening for Acid-Stable Oxygen Evolution Electrocatalysts in the $(Mn-Co-Ta-Sb)O_x$ Composition Space. *Electrocatal.* **2015**, *6* (2), 229−236.
(35) Guevarra, D.; Haber, J. A.; Wang, Y.; Zhou, L.; Kan, K.; Richter, M. H.; Gregoire, J. M. High Throughput Discovery of Complex Metal Oxide Electrocatalysts for the Oxygen Reduction Reaction. *Electrocatal.* **2022**, *13* (1), 1−10.
(36) Tran, K.; Ulissi, Z. W. Active Learning across Intermetallics to Guide Discovery of Electrocatalysts for CO 2 Reduction and H 2 Evolution. *Nat. Catal.* **2018**, *1* (9), 696−703.
(37) Zhong, M.; Tran, K.; Min, Y.; Wang, C.; Wang, Z.; Dinh, C.-T.; De Luna, P.; Yu, Z.; Rasouli, A. S.; Brodersen, P.; Sun, S.; Voznyy, O.; Tan, C.-S.; Askerka, M.; Che, F.; Liu, M.; Seifitokaldani, A.; Pang, Y.; Lo, S.-C.; Ip, A.; Ulissi, Z.; Sargent, E. H. Accelerated Discovery of CO_2 Electrocatalysts Using Active Machine Learning. *Nature* **2020**, *581* (7807), 178−183.
(38) Guevarra, D.; Zhou, L.; Richter, M. H.; Shinde, A.; Chen, D.; Gomes, C. P.; Gregoire, J. M. Materials Structure−Property Factorization for Identification of Synergistic Phase Interactions in Complex Solar Fuels Photoanodes. *npj Comput. Mater.* **2022**, *8* (1), 1−7.
(39) Janet, J. P.; Kulik, H. J. Resolving Transition Metal Chemical Space: Feature Selection for Machine Learning and Structure−Property Relationships. *J. Phys. Chem. A* **2017**, *121* (46), 8939−8954.
(40) Chen, D.; Bai, Y.; Ament, S.; Zhao, W.; Guevarra, D.; Zhou, L.; Selman, B.; van Dover, R. B.; Gregoire, J. M.; Gomes, C. P. Automating Crystal-Structure Phase Mapping by Combining Deep Learning with Constraint Reasoning. *Nat. Mach. Intell.* **2021**, *3* (9), 812−822.
(41) Friedman, J. H. Greedy Function Approximation: A Gradient Boosting Machine. *Ann. Stat.* **2001**, *29* (5), 1189−1232.
(42) Tipping, M. E. Sparse Bayesian Learning and the Relevance Vector Machine. *J. Machine Learning Res.* **2001**, *1*, 211−244.
(43) Pedregosa, F.; Varoquaux, G.; Gramfort, A.; Michel, V.; Thirion, B.; Grisel, O.; Blondel, M.; Prettenhofer, P.; Weiss, R.; Dubourg, V.; Vanderplas, J.; Passos, A.; Cournapeau, D.; Brucher, M.; Perrot, M.; Duchesnay, É. Scikit-Learn: Machine Learning in Python. *J. Machine Learning Res.* **2011**, *12* (85), 2825−2830.
(44) Paszke, A.; Gross, S.; Massa, F.; Lerer, A.; Bradbury, J.; Chanan, G.; Killeen, T.; Lin, Z.; Gimelshein, N.; Antiga, L.; Desmaison, A.; Köpf, A.; Yang, E.; DeVito, Z.; Raison, M.; Tejani, A.; Chilamkurthy, S.; Steiner, B.; Fang, L.; Bai, J.; Chintala, S. PyTorch: An Imperative Style, High-Performance Deep Learning Library. *arXiv (Computer Science.Machine Learning)*, December 3, 2019, 1912.01703. DOI: 10.48550/arXiv.1912.01703.
(45) Breiman, L. Random Forests. *Machine Learning* **2001**, *45* (1), 5−32.
(46) Wang, H.; Abruña, H. D. Designing Synergistic Electrocatalysts for H2 Oxidation and Evolution Reactions in Alkaline Media. *J. Phys. Chem. C* **2021**, *125* (13), 7188−7203.
(47) Sieben, J. M.; Duarte, M. M. E. Nanostructured Pt and Pt−Sn Catalysts Supported on Oxidized Carbon Nanotubes for Ethanol and Ethylene Glycol Electro-Oxidation. *Int. J. Hydrogen Energy* **2011**, *36* (5), 3313−3321.
(48) Ramaswamy, N.; Mukerjee, S. Alkaline Anion-Exchange Membrane Fuel Cells: Challenges in Electrocatalysis and Interfacial Charge Transfer. *Chem. Rev.* **2019**, *119* (23), 11945−11979.
(49) Perez, J.; Paganin, V. A.; Antolini, E. Particle Size Effect for Ethanol Electro-Oxidation on Pt/C Catalysts in Half-Cell and in a Single Direct Ethanol Fuel Cell. *J. Electroanal. Chem.* **2011**, *654* (1−2), 108−115.
(50) Du, M.; Cui, L.; Cao, Y.; Bard, A. J. Mechanoelectrochemical Catalysis of the Effect of Elastic Strain on a Platinum Nanofilm for the ORR Exerted by a Shape Memory Alloy Substrate. *J. Am. Chem. Soc.* **2015**, *137* (23), 7397−7403.

https://doi.org/10.1021/acssuschemeng.2c05170
ACS Sustainable Chem. Eng. XXXX, XXX, XXX−XXX

(51) Tsiakaras, P. E. PtM/C (M = Sn, Ru, Pd, W) Based Anode Direct Ethanol−PEMFCs: Structural Characteristics and Cell Performance. *J. Power Sources* **2007**, *171* (1), 107−112.
(52) Bergamaski, K.; Gonzalez, E. R.; Nart, F. C. Ethanol Oxidation on Carbon Supported Platinum-Rhodium Bimetallic Catalysts. *Electrochim. Acta* **2008**, *53* (13), 4396−4406.
(53) Solla-Gullón, J.; Vidal-Iglesias, F. J.; Montiel, V.; Aldaz, A. Electrochemical Characterization of Platinum−Ruthenium Nanoparticles Prepared by Water-in-Oil Microemulsion. *Electrochim. Acta* **2004**, *49* (28), 5079−5088.
(54) Du, W.; Yang, G.; Wong, E.; Deskins, N. A.; Frenkel, A. I.; Su, D.; Teng, X. Platinum-Tin Oxide Core−Shell Catalysts for Efficient Electro-Oxidation of Ethanol. *J. Am. Chem. Soc.* **2014**, *136* (31), 10862−10865.
(55) Roth, C.; Goetz, M.; Fuess, H. Synthesis and Characterization of Carbon-Supported Pt−Ru−WOx Catalysts by Spectroscopic and Diffraction Methods. *J. Appl. Electrochem.* **2001**, *31* (7), 793−798.
(56) Rodriguez, J. A.; Campbell, R. A.; Goodman, D. W. The Nature of Metal-Metal Bonding at Bimetallic Interfaces. *Surf. Sci.* **1994**, *307*−*309*, 377−383.
(57) Zheng, J.; Cullen, D. A.; Forest, R. V.; Wittkopf, J. A.; Zhuang, Z.; Sheng, W.; Chen, J. G.; Yan, Y. Platinum−Ruthenium Nanotubes and Platinum−Ruthenium Coated Copper Nanowires As Efficient Catalysts for Electro-Oxidation of Methanol. *ACS Catal.* **2015**, *5* (3), 1468−1474.
(58) Shukla, A. K.; Aricò, A. S.; El-Khatib, K. M.; Kim, H.; Antonucci, P. L.; Antonucci, V. An X-Ray Photoelectron Spectroscopic Study on the Effect of Ru and Sn Additions to Platinised Carbons. *Appl. Surf. Sci.* **1999**, *137* (1), 20−29.
(59) Ramallo-López, J. M.; Santori, G. F.; Giovanetti, L.; Casella, M. L.; Ferretti, O. A.; Requejo, F. G. XPS and XAFS Pt L2,3-Edge Studies of Dispersed Metallic Pt and PtSn Clusters on SiO2 Obtained by Organometallic Synthesis: Structural and Electronic Characteristics. *J. Phys. Chem. B* **2003**, *107* (41), 11441−11451.
(60) Shen, S. Y.; Zhao, T. S.; Xu, J. B. Carbon Supported PtRh Catalysts for Ethanol Oxidation in Alkaline Direct Ethanol Fuel Cell. *Int. J. Hydrogen Energy* **2010**, *35* (23), 12911−12917.
(61) Chen, J.; Yiu, Y. M.; Wang, Z.; Covelli, D.; Sammynaiken, R.; Finfrock, Y. Z.; Sham, T.-K. Elucidating the Many-Body Effect and Anomalous Pt and Ni Core Level Shifts in X-Ray Photoelectron Spectroscopy of Pt−Ni Alloys. *J. Phys. Chem. C* **2020**, *124* (4), 2313−2318.
(62) Hammer, B.; Nørskov, J. K. Theory of Adsorption and Surface Reactions. In *Chemisorption and Reactivity on Supported Clusters and Thin Films: Towards an Understanding of Microscopic Processes in Catalysis*; Lambert, R. M., Pacchioni, G., Eds.; NATO ASI Series 331; Springer: Dordrecht, Netherlands, 1997; pp 285−351. DOI: 10.1007/978-94-015-8911-6_11.
(63) Hammer, B.; Norskov, J. K. Why Gold Is the Noblest of All the Metals. *Nature* **1995**, *376* (6537), 238−240.
(64) Stamenkovic, V. R.; Mun, B. S.; Arenz, M.; Mayrhofer, K. J. J.; Lucas, C. A.; Wang, G.; Ross, P. N.; Markovic, N. M. Trends in Electrocatalysis on Extended and Nanoscale Pt-Bimetallic Alloy Surfaces. *Nat. Mater.* **2007**, *6* (3), 241−247.
(65) Lee, K.-S.; Jeon, T.-Y.; Yoo, S. J.; Park, I.-S.; Cho, Y.-H.; Kang, S. H.; Choi, K. H.; Sung, Y.-E. Effect of PtRu Alloying Degree on Electrocatalytic Activities and Stabilities. *Appl. Catal. B: Environmental* **2011**, *102* (1), 334−342.
(66) Yang, B.; Lu, Q.; Wang, Y.; Zhuang, L.; Lu, J.; Liu, P.; Wang, J.; Wang, R. Simple and Low-Cost Preparation Method for Highly Dispersed PtRu/C Catalysts. *Chem. Mater.* **2003**, *15* (18), 3552−3557.
(67) Siri, G. J.; Ramallo-López, J. M.; Casella, M. L.; Fierro, J. L. G.; Requejo, F. G.; Ferretti, O. A. XPS and EXAFS Study of Supported PtSn Catalysts Obtained by Surface Organometallic Chemistry on Metals: Application to the Isobutane Dehydrogenation. *Appl. Catal. A: General* **2005**, *278* (2), 239−249.
(68) Hu, Z.; Allen, F. M.; Wan, C. Z.; Heck, R. M.; Steger, J. J.; Lakis, R. E.; Lyman, C. E. Performance and Structure of Pt−Rh Three-Way Catalysts: Mechanism for Pt/Rh Synergism. *J. Catal.* **1998**, *174* (1), 13−21.
(69) Zhang, Y.; Janyasupab, M.; Liu, C.-W.; Li, X.; Xu, J.; Liu, C.-C. Three Dimensional PtRh Alloy Porous Nanostructures: Tuning the Atomic Composition and Controlling the Morphology for the Application of Direct Methanol Fuel Cells. *Adv. Funct. Mater.* **2012**, *22* (17), 3570−3575.
(70) Silva, J. C. M.; Assumpção, M. H. M. T.; Hammer, P.; Neto, A. O.; Spinacé, E. V.; Baranova, E. A. Iridium−Rhodium Nanoparticles for Ammonia Oxidation: Electrochemical and Fuel Cell Studies. *ChemElectroChem.* **2017**, *4* (5), 1101−1107.
(71) Kulkarni, A.; Siahrostami, S.; Patel, A.; Nørskov, J. K. Understanding Catalytic Activity Trends in the Oxygen Reduction Reaction. *Chem. Rev.* **2018**, *118* (5), 2302−2312.
(72) Zhou, W. Pt Based Anode Catalysts for Direct Ethanol Fuel Cells. *Appl. Catal. B: Environmental* **2003**, *46* (2), 273−285.
(73) Yano, J.; Gaffney, K. J.; Gregoire, J.; Hung, L.; Ourmazd, A.; Schrier, J.; Sethian, J. A.; Toma, F. M. The Case for Data Science in Experimental Chemistry: Examples and Recommendations. *Nat. Rev. Chem.* **2022**, *6*, 357−370.

https://doi.org/10.1021/acssuschemeng.2c05170
ACS Sustainable Chem. Eng. XXXX, XXX, XXX−XXX